coatings

MDPI

Article

Corrosion Testing of Thermal Spray Coatings in a Biomass Co-Firing Power Plant

Maria Oksa *, Jarkko Metsäjoki and Janne Kärki

VTT Technical Research Centre of Finland Ltd., P.O. Box 1000, FI-02044 VTT, Finland; jarkko.metsajoki@vtt.fi (J.M.); janne.karki@vtt.fi (J.K.)

* Correspondence: maria.oksa@vtt.fi; Tel.: +358-50-5365844

Academic Editor: Pedro Neto

Received: 20 September 2016; Accepted: 19 November 2016; Published: 24 November 2016

Abstract: Large-scale use of biomass and recycled fuel is increasing in energy production due to climate and energy targets. A 40% cut in greenhouse gas emission compared to 1990 levels and at least a 27% share of renewable energy consumption are set in EU Energy Strategy 2030. Burning fuels with high content of corrosive species such as chlorine and heavy metals causes deterioration of boiler components, shortened lifetime, limited availability of a plant and hence higher maintenance and investment costs and lower thermal and economic efficiency. Coatings can be applied to protect the critical boiler components against high temperature corrosion. In this study, five thermal spray coatings were tested in an actual biomass co-firing boiler for 1300 h with a measurement probe. The coatings were analyzed after the exposure by metallographic means and scanning electron microscope/energy-dispersive X-ray spectroscope (SEM/EDX). The deposits formed on the specimens were analyzed by X-ray fluorescence. At 550 °C, the coatings showed excellent corrosion performance compared to reference material ferritic steel T92. At 750 °C, tube material A263 together with NiCr and NiCrTi had the highest corrosion resistance. To conclude, thermal spray coatings can offer substantial corrosion protection in biomass and recycled fuel burning power plants.

Keywords: thermal spray; coating; corrosion; high temperature; protection; boiler

1. Introduction

Response to the threat of climate change has taken a major step with the Paris Agreement [1], which is an extensive and legally binding climate agreement with target of holding global warming well below 2 °C compared to pre-industrial levels. For the first time, almost all countries around the world have agreed to take actions to combat climate change. Energy and climate targets to prevent greenhouse gas emissions have been tightened from the 20-20-20 targets, including 20% cut in greenhouse gas emissions from 1990 levels, 20% of EU energy from renewables and 20% improved in energy efficiency, to 2030 targets of a 40% cut in the greenhouse gas emissions and at least 27% share of renewable energy consumption [2]. While share of wind and solar energy are increasing rapidly, other renewable energy forms producing base load are needed, during and beyond the transformation period until the year 2050, when 26% to 29% of global electricity is predicted to be produced by wind and solar power [3,4]. Bioenergy, especially production of thermal energy by biomass, is currently the largest form of renewable energy and is expected to keep its dominant position. However, biomass combustion together with enhanced recycled fuel (waste) combustion is detrimental to components of the power plants due to very reactive species that cause slagging and high temperature corrosion.

Severe fireside corrosion, encountered especially in boilers using biomass and recycled fuel, occurs when chemical reactions with the combustion gases and deposits at high temperatures cause the loss of heat exchanger surfaces, e.g., superheaters. It is often caused by a gaseous or molten attack

induced by compounds of chlorine, bromine, alkali metals (K, Na), sulfur, and heavy metals (Zn, Pb, Cu, etc.) [5–8]. Corrosion may cause a leakage, which leads to a shut-down of the boiler and hence severe costs by reduced availability and repair [9]. Other than using higher alloyed steels or nickel-based alloy tubes, thermal spray coatings can be applied to low alloyed tubes for corrosion protection with economical cost and high thermo-mechanical properties. In thermal spraying, the coating is formed from molten or semi-melted droplets producing a lamellar structure. High velocity spray methods generate coatings with good adhesion and low porosity [10], which are essential for sufficient protection of the substrate material. Thermal spray coatings have proven their ability for corrosion protection in laboratory tests, e.g., plasma sprayed NiCr coating against high temperature corrosion under deposits simulating conditions of coal-biomass firing [11]. The performance was strongly dependent on the amount of the chromium in the coating, as the corrosion protection took place by a protective chromium oxide layer.

In this study, five thermal spray coatings were tested in a co-firing biomass boiler for 1300 h, up to 750 °C material temperatures, with a measurement probe in order to validate the corrosion performance in actual conditions [12]. As reference, ferritic steel and nickel based alloys were exposed to the same conditions.

2. Materials and Methods

High temperature corrosion performance of five thermal spray coatings were tested in a biomass co-fired circulating fluidized bed boiler for about 1300 h with a controlled probe measurement. Two tube metal alloys were used as reference materials. Test temperatures for the materials were 550 °C and 750 °C.

2.1. Thermal Spray Coatings

Five thermal spray coatings were manufactured for high temperature corrosion exposure in a biomass co-firing boiler. Four of the coatings were sprayed by high velocity oxy-fuel (HVOF) method, and one with a wire arc. The coating was performed on two substrate materials. The coating materials were nickel based powders Ni-980-1/1260F from Praxair (NiCr), Diamalloy 1005 from Sulzer Metco (IN625) and Diamalloy 4006 from Sulzer Metco (NiCrW), a wire TAFA Nickel Chrome 45 CT from Praxair (NiCrTi), and an iron based powder SHS9172 from Nanosteel (FeCr). The substrate materials were a ferritic steel T92 (ASTM A213 T92) and a nickel super alloy A263 (NIMONIC® Alloy 263, Special Metals, Hereford, UK). Chemical composition of the coating and substrate materials are presented in Table 1.

Table 1. Chemical composition of the coating and substrate materials (wt.%).

Material	Ni	Cr	Fe	Mo	W	Co	Nb	Si
NiCr	Bal.	>45	1.1	–	–	–	–	2.1
IN625	Bal.	21.5	2.5	9.0	–	–	3.7	0.2
NiCrW	Bal.	20.5	<1.0	9.0	10.0	–	–	–
FeCr	–	<25.0	Bal.	<6.0	<15.0	–	<12.0	<2.0
NiCrTi	Bal.	42–46	–	–	–	–	–	–
T92	–	8–9.5	Bal.	0.3–0.6	1.5–2	–	–	≤0.5
A263	Bal.	19–21	<0.7	5.6–6.1	–	19–21	–	<0.4
Material	**Mn**	**Cu**	**Al**	**Ti**	**V**	**C**	**B**	
NiCr	–	–	–	–	–	–	–	
IN625	0.1	–	–	–	–	–	–	
NiCrW	–	4.0	–	–	–	0.75	0.75	
FeCr	<3.0	–	–	–	–	<4.0	<5.0	
NiCrTi	–	–	–	0.3–1	–	–	–	
T92	0.3–0.6	–	≤0.4	–	0.15–0.25	0.07–0.013	–	
A263	<0.6	–	<0.6	1.9–2.4	–	0.04–0.08	–	

The coating was performed on the perimeter of tube rings with size of Φ 48 mm × 12.5 mm for exposure at 550 °C, and Φ 34 mm × 15 mm for 750 °C. HVOF process with CJS (Carbide Jet Spray by Thermico GmbH & Co KG, Dortmund, Germany) spray gun was used for spraying the powders. Depending on process parameters, CJS produces high velocity and low thermal input on the sprayed powders, generating thick coatings with low oxidation rate and good adhesion to the substrate material. However, small particle size would be optimal for CJS to enhance the melting of the powder particles and hence sufficient cohesion between the lamellas. In this study, the applied powders were designed for a previous generation spray gun (e.g., Diamond Jet Hybrid from Sulzer Metco, Westbury, NY, USA), and therefore slightly too coarse for the used method. Arc spraying was performed with Smart Arc (by Sulzer Metco). The process parameters of the spraying are presented in Table 2. Powder feed rate was 50 g/min for HVOF and applied spraying distance was 250 mm. For arc spraying, the spraying distance was 150 mm. Images of the cross-section of the coated specimens are presented in Figure 1. Both NiCr and IN625 showed reasonably large lamellas with very little oxidation in the lamellar boundaries, whereas the arc sprayed NiCrTi was highly oxidized (darker areas in the micrograph) with fully molten structure.

Table 2. Process parameters for high velocity oxy-fuel (HVOF) spraying (L/min). Below: process parameters for arc spraying.

Coating	Spray Method	H_2	Kerosene	O_2	N_2	Sweeps	Thickness (µm)
NiCr	CJS, 140 mm	100	16	1000	6 + 6	14	130
IN625	CJS, 140 mm	100	16	1000	6 + 6	10	140
NiCrW	CJS, 140 mm	100	16	1000	6 + 6	20	270
FeCr	CJS, 140 mm	100	16	850	6 + 6	21	200
Coating	**Spray Method**	**Voltage**	**Current**	**Air**			**Thickness (µm)**
NiCrTi	Smart Arc	30 V	220 A	3.5/2.5 bar			180

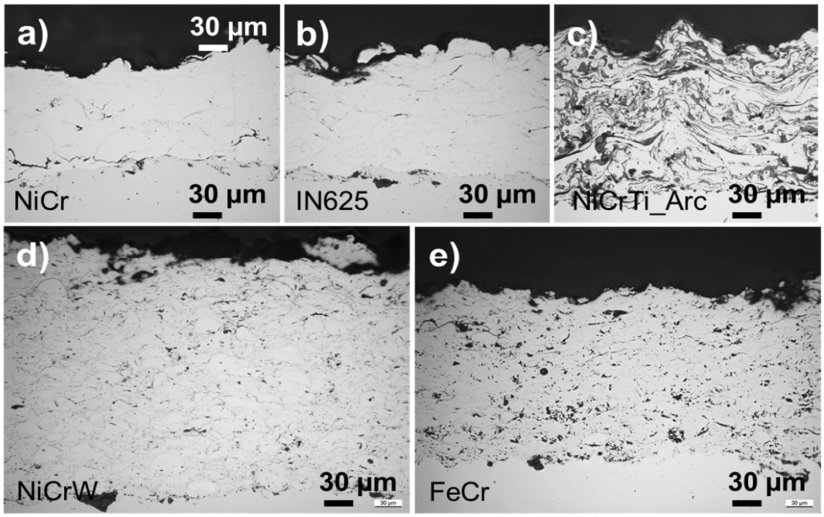

Figure 1. Optical micrographs of the thermal spray coatings before testing: (**a**) HVOF sprayed NiCr and (**b**) IN625; (**c**) arc sprayed NiCrTi; (**d**) HVOF sprayed NiCrW and (**e**) FeCr.

Porosity of the coatings was measured with image analysis from optical micrographs. Oxides at lamellar boundaries and pull-outs due to specimen preparation may influence to the image analysis results. According to the analysis, the most dense coating was HVOF sprayed NiCrW with 2.6% porosity. Porosity of other HVOF-sprayed coatings varied from 3.3% for NiCr, 4.8% for IN625 to 5.8% for FeCr coating. Arc sprayed NiCrTi had porosity of about 4.6%.

2.2. Measurement Probe

Measurement probes can be applied for corrosion monitoring and deposit analysis in high temperature combustion plants. They can be used for analyzing both short- and long-term deposition build-up and corrosion risks. An advanced water-air-cooled probe was developed to test materials in two different temperatures. The probe is approximately two meters in length and can accommodate two sections with six test rings in each. One section is water- and air-cooled and is exposed at metal temperatures of approximately 550 °C and the second is air-cooled at metal temperatures around 750 °C. The probe with two separate sample regions is presented in Figure 2.

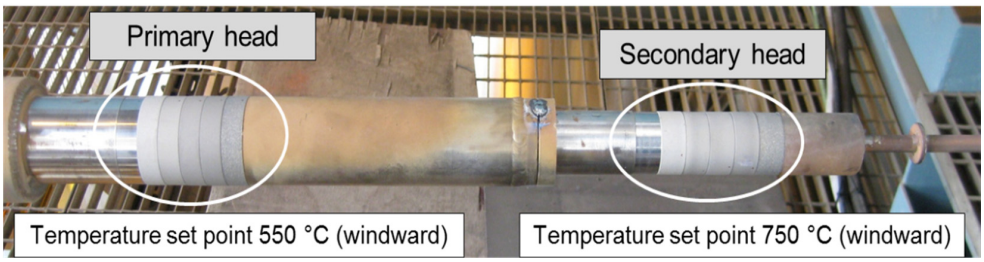

Figure 2. High temperature probe for corrosion testing at two temperature regions.

There are several temperature measurements in different sides of the probe for both temperature areas. The primary head consists of a stationary part, which has four thermo-couples and area for detachable material rings. The width of a detachable material ring in the primary head is 12.5 mm/each. In the secondary head, the detachable material rings are connected to the system through a separate extension ring. The width of a detachable material ring in the secondary head is 15 mm/each. There are two thermo-couples in the extension ring and material temperatures of the detachable material rings are measured at three rings. The flue gas temperature is measured in the tip of the probe with one covered thermo-couple. The thermal expansion in primary and secondary heads as well as in the casing is eliminated with a special spring system consisting of four separate springs.

The probe is air- and water-cooled with a separate controllable cooling unit. During the tests the two meter casing remains cool by water cooling whereas the temperatures of the sample exposure heads are adjusted as desired by additional air cooling. The surface temperatures of the probes vary depending on the direction of the flue gas flow. During the insertion of the probe into the boiler, the direction is chosen so that the windward (i.e., against the flue gas flux) temperature in the sample ring area is maintained constant by adjusting the air cooling rate. The temperatures on the other sides of the probe vary depending on the deposit formation and cleaning stages.

2.3. Test Facility—The Biomass Co-Firing Plant

The probe exposure trial was performed at the Alholmens Kraft power plant located in the western coast region of Finland, in the town of Pietarsaari. The facility is one of the largest biomass fueled power plants in the world producing electricity, district heating and process steam and heat for the UPM-Kymmene plant. The exposure involved deployment of the corrosion probe in a 550 MW_{th} circulating fluidized bed boiler, which has live steam parameters of 194 kg/s, 165 bar, 545 °C. During the measurements the boiler was fired on average with 30% peat, 10% coal, 50% of biomass (forest residues, industrial wood and bark etc.) and 10 % SRF (solid recovered fuel). Daily fluctuations in the fuel shares in comparison to those averages can be wide as well as the fluctuations in the whole process parameters. The probe was inserted into the superheater area after the cyclones.

2.4. Specimen Characterization

After the exposure the coated and reference ring specimens were removed from the probe and embedded in cold setting resin on site. The embedded specimens were cross-sectioned by grinding

with ethanol followed by polishing. The cross-sections were studied by an optical microscope and a scanning electron microscope (SEM) (FEI/Philips XL30 ESEM, FEI, Eindhoven, The Netherlands) equipped with energy-dispersive X-ray spectroscope (EDX) (UltraDry EDS Detector, Thermo Fisher Scientific Inc., Waltham, MA, USA) for elemental analysis and mapping. Separate deposit samples were detached from the probe near the test samples and they were analyzed by X-ray fluorescence (XRF) using the Philips PW2404 X-ray spectrometer and semiquantitative SemiQ program (PANalytical, Almelo, The Netherlands). The samples were analyzed for fluorine (F) and heavier elements excluding noble gases. The detection limit of the method is typically in the order of 0.01 wt.%.

3. Results

3.1. Process and Probe Measurement Data

Plant electricity output varied a lot in short intervals depending on the electricity markets, which had a strong effect on the flue gas temperatures inside the boiler, and further on the temperatures at the probe surfaces, Figure 3a. Some fluctuations were also present in the flue gas emissions, e.g., the HCl and SO_2 emissions presented in Figure 3b. Due to high variations in the plant load and process temperatures, the probe temperature profiles were fluctuating as well, which influenced the stability of the controlled temperature on the windward surface, as presented in Figure 4a. Hence, the actual material temperatures were lower than planned: 536 °C for the primary and 697 °C for the secondary head in the windward side on average. For the leeward side, the average temperatures were 502 °C for the primary and 609 °C for the secondary head. Minimum values in the probe were in the leeward side; 331 °C for the primary and 566 °C for the secondary head. The maximum values in the windward side were 602 °C (primary) and 764 °C (secondary head). The temperatures are presented in the form of a stability curve, where the fluctuations, which followed the flue gas temperature, are not shown. The diagram shows overall temperature behavior to the exposure period, but not in a chronological order. Three short temperature and pressure changes occurred in the probe during the test period due to shutting the cooling water circulation and cleaning the filter. Operational thermal cycling (627–874 °C flue gas) was caused by the electric output variation. After the exposure, the material testing probe was covered with a light brown deposit, which had partly detached. The probe is presented in Figure 4b.

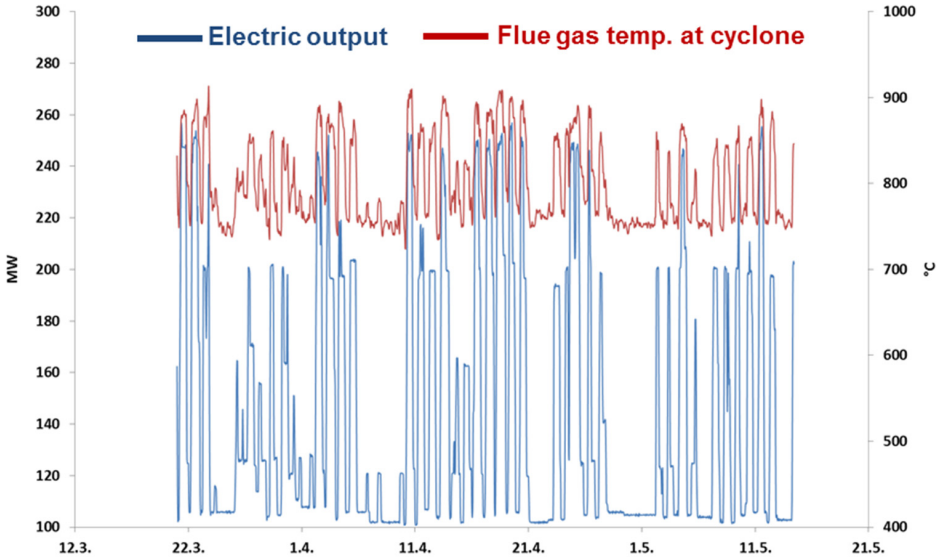

(**a**)

Figure 3. *Cont.*

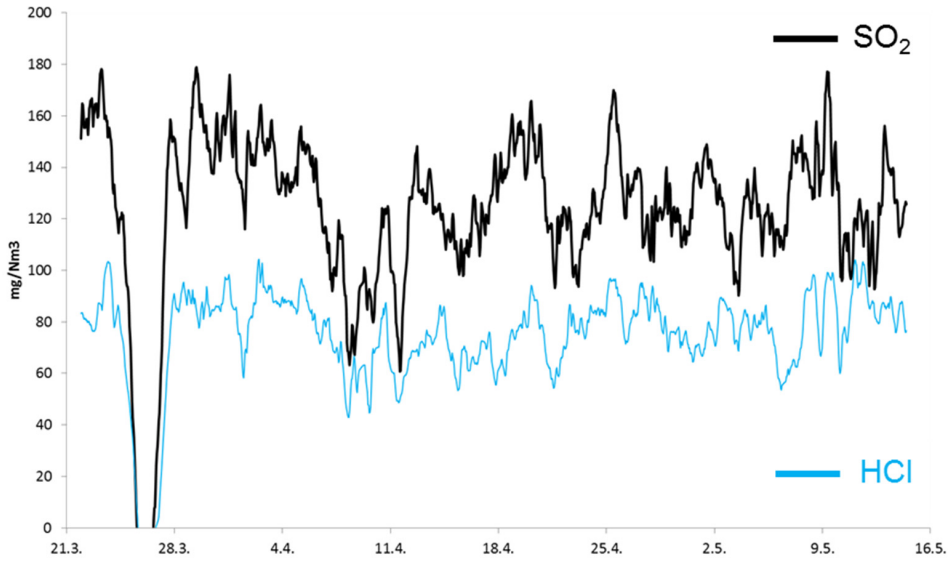

(**b**)

Figure 3. Process data during the test exposure: (**a**) Plant electricity output (MW) and flue gas temperature (°C) at the cyclone; (**b**) Flue gas data of sulfur dioxide SO_2 and hydrogen chloride HCl during the test (mg/Nm^3).

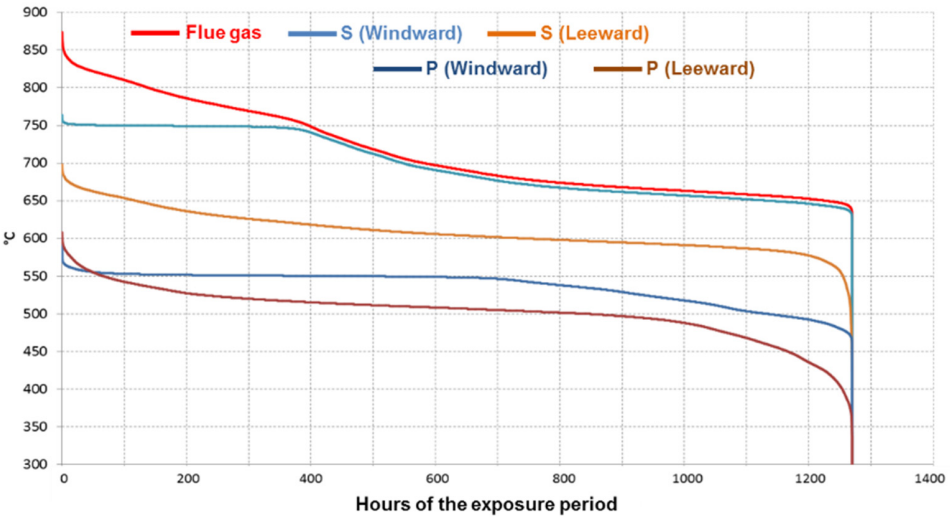

(**a**)

(**b**)

Figure 4. (**a**) Probe measurement data presented in the form of stability curve for flue gas, windward and leeward temperatures (°C) (S = secondary head, P = primary head); (**b**) Probe after the 1300 h exposure, material samples at metal temperatures of approximately 550 °C.

3.2. Formed Deposits

The deposit after the exposure was light brown and easily detachable from the probe. At 750 °C probe section, the deposit layer was slightly thicker compared to the lower temperature section. Deposits were composed mainly of sulfur, calcium, potassium, silicon, sodium, iron and aluminum, as presented in Table 3. Other elements in the deposit were magnesium, phosphorus, titanium and manganese. The amount of zinc was considerable (0.4/0.7 wt.%) in the analyzed deposits. At the lower temperature, amounts of sulfur, potassium and sodium were higher compared to the 750 °C temperature. At the higher temperature, no chlorine was detected in the deposit.

Table 3. Composition of the formed deposits on the probe sections at 550 °C and 750 °C (wt.%).

Element	S	Ca	K	Si	Na	Fe	Al	Mg	P	Ti
550 °C	14	10	14	4.5	5.7	4.2	2.7	1.1	0.78	0.7
750 °C	11	10	9.8	9.7	1.6	5.2	4.7	0.91	0.91	0.84
Element	**Zn**	**Mn**	**Ba**	**Cu**	**Pb**	**Sr**	**Cr**	**Rb**	**Cl**	**Ni**
550 °C	0.42	0.38	0.3	0.12	0.08	0.06	0.15	0.06	0.05	0.03
750 °C	0.71	0.29	0.23	0.06	0.12	0.05	0.09	0.07	–	0.02

3.3. Corrosion Resistance at 550 °C

All the coated specimens showed high corrosion resistance against the biomass co-firing conditions and endured the exposure at 550 °C without significant changes, whereas the uncoated substrate material steel T92 had corroded strongly during the exposure. IN625 coating had minor corrosion within the top 20 µm of the coating at the flue gas side. Figure 5 presents SEM images of T92, NiCr and IN625 after the exposure. NiCrW, IN625, NiCr and NiCrTi had formed a 1–2 µm thin Cr rich oxide layer, which protected against corrosion.

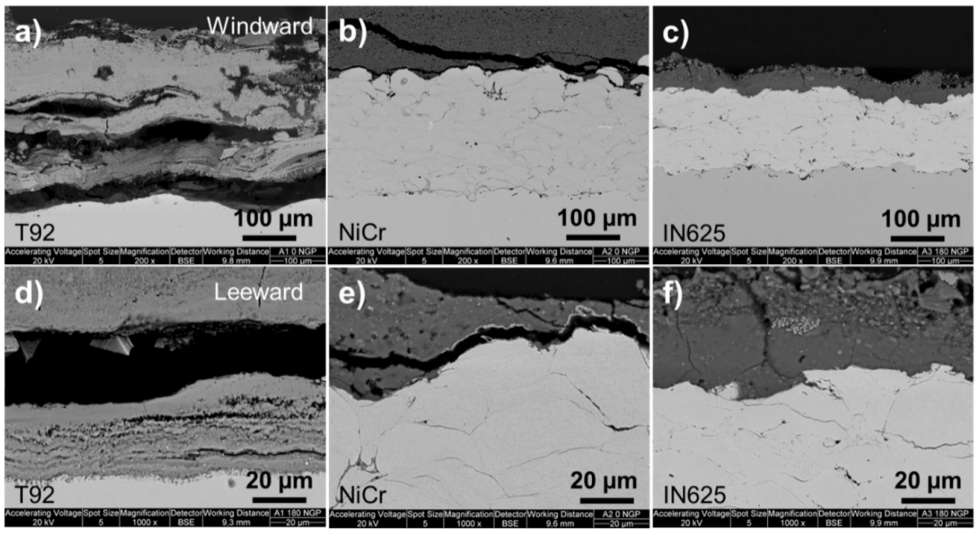

Figure 5. SEM (BSE–Back scattered electron) images of the cross-section of the specimens after the 1300 h exposure at 550 °C: (**a**–**c**) Windward side of T92, NiCr and IN625 coatings; (**d**–**f**) Same materials at the leeward side.

FeCr was found to be corroded at the side of 90° from the flue gas direction and it peaked at the leeward side (i.e., opposite to the flue gas flux), Figure 6, with a 30 µm thick corrosion product layer and internal coating degradation up to 20–40 µm depth. Chlorine was detected at the outer surface of the FeCr coating in the leeward side. According to the EDX point analysis (wt.%), the separate chlorine

containing areas on the coating (one marked with an arrow in Figure 6) contained 7.3% Cl, 50.2% iron, 24.1% oxygen, 9.1% chromium. There was also tungsten (5.2%), niobium (3.1%), aluminum and silicon (0.5 % each). In the internal degradation area, composition included Fe (44.1%), Cr (23.1%), W (11.9%), O (8.9%), Nb (8.3%), Si (1.8%), Cl (1.1%), Al (0.6%), and K (0.2%). Chlorine had formed a thin, about 5 µm in thickness, mixed iron-chromium chlorine-oxide layer on the surface of the coating. Right next to the coating, this layer contained Cr (22.3%), O (18.2%), Mo (19.3%), W (13.7), Fe (10.7%), Si (8.5%), Cl (5.1%), Al (1.9%), and K (0.4%). At about 3 µm from the coating surface, the layer consisted of Cr (47.9%), O (25.6%), Fe (15.7%), Zn (2.3%), S (2.2%), Mg (1.6%), K (1.4%), Al (1.0%), Cl (1.0%), P (0.4%), Ti (0.4%) and Si (0.3%).

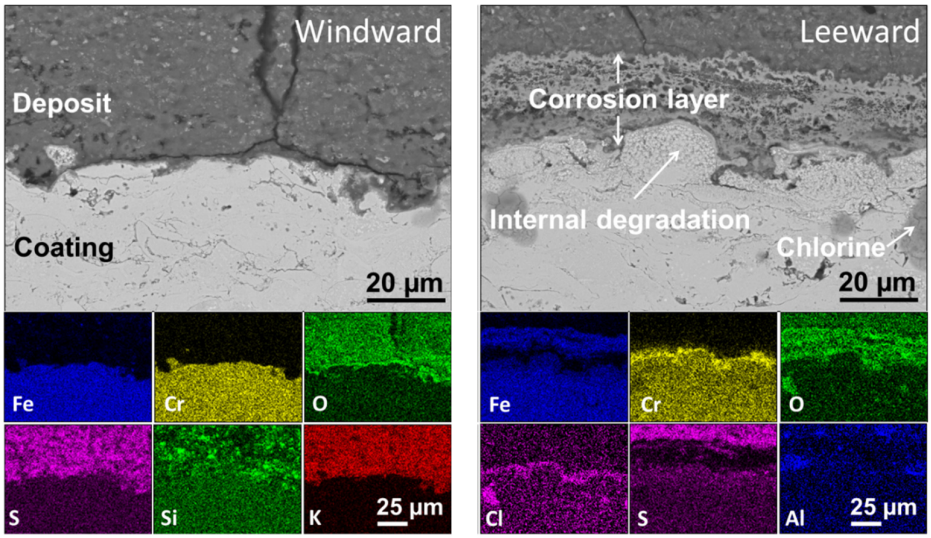

(**a**) (**b**)

Figure 6. SEM (BSE) image of the outer surface of the FeCr coating and energy-dispersive X-ray spectroscope (EDX) map analysis from the windward (**a**) and leeward side (**b**).

The uncoated T92 steel had up to 200 µm thick corrosion product layer both at the windward and leeward side, as presented in Figure 7. The multilayered oxide iron-chromium oxide was porous and partly detached from the metal surface. Next to the metal, internally grown mixed iron and chromium oxide was comprised from several layers. A dense oxide containing a higher amount of chromium was detected above it, and the most outer iron oxide layer was mixed with the deposit, containing mainly oxygen, iron, sulfur, calcium, potassium, aluminum and silicon.

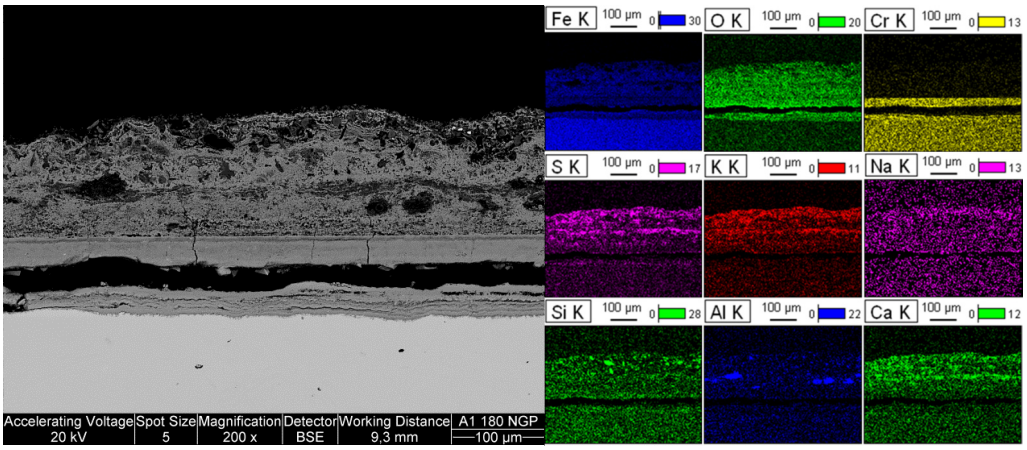

Figure 7. SEM (BSE) image of the T92 uncoated tube material with EDX mapping from the leeward side.

3.4. Corrosion Resistance at 750 °C

The coatings exposed at 750 °C showed distinct differences between the coatings and also between locations within the specimens. Generally the flue gas direction had the most severe corrosion and the leeward direction the least. The uncoated substrate material A263 had formed a 1–10 µm thin Cr-rich oxide scale, where 10 µm represents slight pitting. On average, the scale was around 3 µm thin. On the windward side, the protective oxide layer was dense and uniform. The scale was observed to be thickest at the leeward orientation. S, Ti and Al were found in the Cr-rich oxide scale. A thin porous oxide layer above the chromium oxide layer, shown with an arrow in Figure 8, contained mainly nickel, oxygen and iron, but also sodium (2.4 wt.%), sulfur (2.1 wt.%) and zinc (1.8 wt.%). Traces of chlorine (0.2 wt.%) were detected only in the deposit layer. Deepest penetration into the material through grain boundaries was 10 µm.

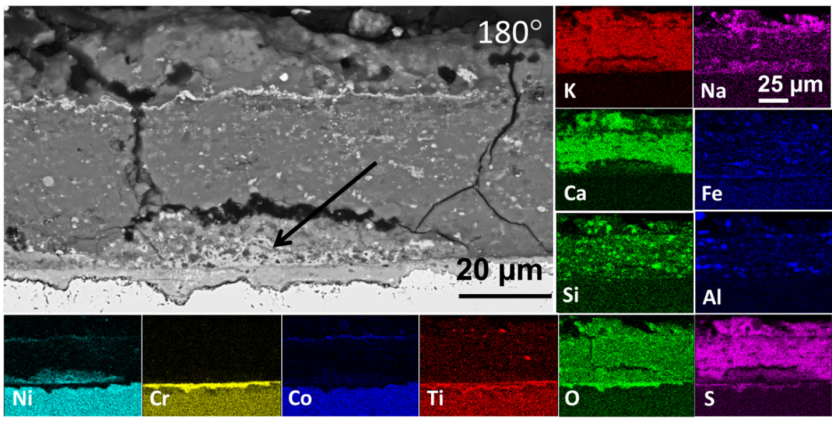

Figure 8. SEM (BSE) image of the metal surface of A263 nickel alloy and EDX map analysis from the leeward side. The arrow pointing to the porous oxide scale containing zinc.

NiCr coating had formed a thin, 2 µm thick layer on the coating, Figure 9. EDX analysis revealed that the thin layer contained high amounts of chromium and oxygen. EDX mapping confirmed that the thin layer had protected the coating against the environment: The coating forming elements Ni and Cr were not found on the deposits, which contained mainly K, Ca and Na along with S and O.

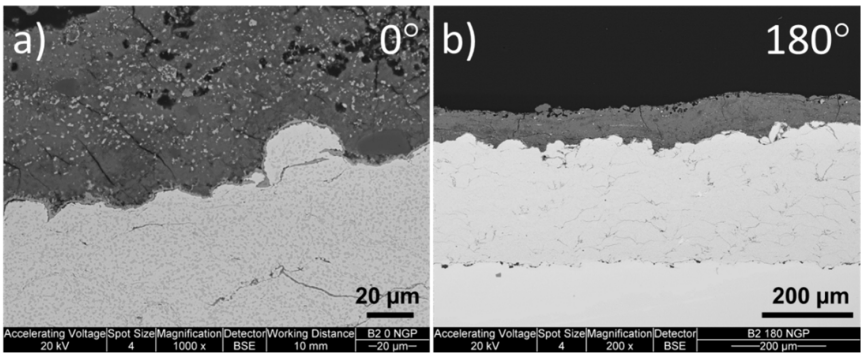

Figure 9. SEM (BSE) images of NiCr coating after the exposure at 750 °C for 1300 h: (**a**) windward and (**b**) leeward side.

IN625 coating exhibited pit corrosion not only at flue gas direction but also at side areas of the test ring. In many cases, the corrosion had already reached the substrate and continued deeper into it and also widened the pit. One such location was at the windward side, where the coating had been completely lost over a wide area and pits could be seen where there was still coating left. Figure 10 shows the remaining coating at windward orientation.

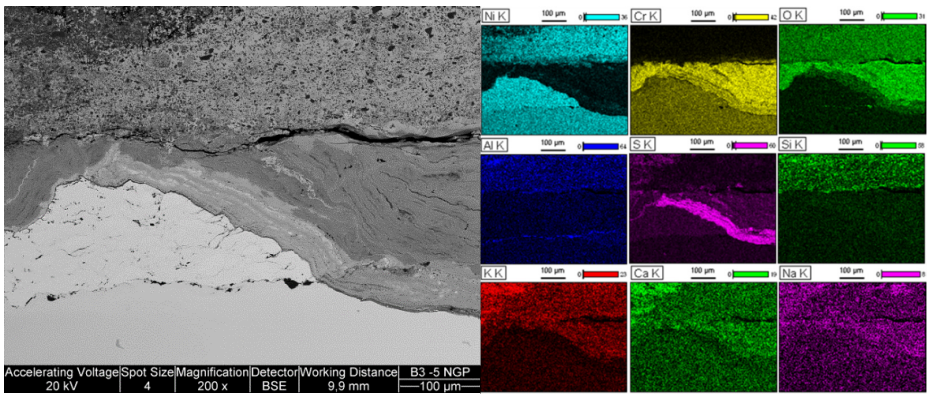

Figure 10. SEM (BSE) image of the remains of the IN625 coating and EDX map analysis from the windward side.

FeCr coating hade corroded rather uniformly. The highest corrosion rate was at the windward side with a 25–55 µm thick corrosion product that consisted of two irregular layers: topmost being porous iron oxide rich layer, which was partially mixed with the deposit. A porous Cr and Nb rich layer was under the topmost layer. The thickest parts of the corrosion product had the least dense Cr-layer. At leeward and side orientations, the thickness of the corrosion product layer was around 20 µm.

NiCrW coating was completely consumed on the flue gas orientation, but the corrosion products and deposits were unfortunately lost during removal of the specimen from the probe. Prior to the removal, it was observed that the deposits around the specimen were massively bulging, unlike on the other specimens. At the side area, some corrosion products were found. EDX analyses revealed that they were related to the corrosion of the substrate material, which indicates that the coating had been completely lost, even before the unfortunate spallation during specimen removal. At the leeward direction, a short piece of coating was found. The thickness of the remaining coating was 80 µm, of which 30 µm was badly degraded. EDX analyses showed that oxygen had penetrated the coating and formed a layer with chromium next to the substrate. Nevertheless, sulfur had not been able to penetrate the coating and was found only in the severely degraded topmost 30 µm.

The only arc sprayed coating, NiCrTi, had uniform corrosion throughout the coating surface. EDX analyses revealed that the coating forming elements were protected by a Cr-rich layer on top of the coating. The thickness of the Cr and O-rich layer was at times up to 20 µm, but generally around 2–4 µm. It is worth noting that, due to the arc spraying method, the coating was moderately pre-oxidized: Oxidation at the lamella boundaries is clearly visible in the elemental maps of Figure 11. Sulphur was unable to penetrate the coating.

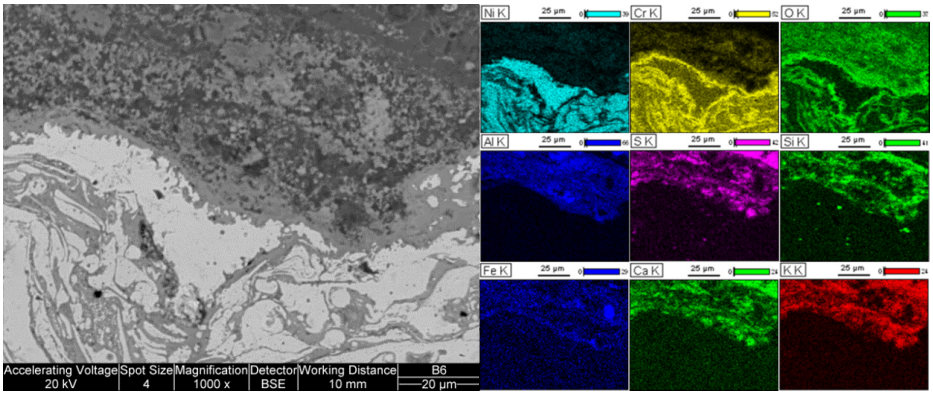

Figure 11. SEM (BSE) image of the outer surface of the arc sprayed NiCrTi coating and EDX map analysis from the leeward side.

4. Discussion

An exposure campaign with corrosion probe was conducted in a 550 MW_{th} (produced thermal power) circulating fluidized bed boiler at Alholmens Kraft power plant. During this 1300 h test exposure, the samples with five thermal spray coatings NiCr, IN625, NiCrW, FeCr and NiCrTi were exposed at two metal temperature ranges of 550 and 750 °C together with reference tube materials ferritic steel T92 and nickel super alloy A263. Due to high variations in the plant load and process temperatures the probe temperature profiles were fluctuating and also fluctuations in the fuel shares were wide. In this context the effects of fuels and boiler process parameters on corrosion phenomena were not straightforward. However, the relatively high peak and average temperatures in the probe surface and the high shares of biomass and SRF fuels used in the boiler sustained the risks for corrosion phenomena, which were shown also in the analyzed samples.

The coating performance at 550 °C was excellent compared to the ferritic tube material T92. The corrosion layer thicknesses of the coatings were about 1/7 or negligible compared to the corrosion layer thickness of the T92. The corrosion rates of the coatings varied between 1–5 μm/1000 h in the windward side and 1–31 μm/1000 h in the leeward side at lower test temperature. The corresponding corrosion rates of T92 steel were 186 μm/1000 h and 275 μm/1000 h. The corrosion mechanism differed at 550 °C in the FeCr coating between the different sides: only minor corrosion was detected in the windward side, whereas in the leeward side the corrosion was pronounced. The non-protective layer that formed in the leeward side may have been caused by lower material temperature, which allowed zinc to deposit on the coating, which reacted with chlorine, chromium and iron, forming low melting compounds and hence causing stronger corrosion. Zinc can condensate on heat transfer surfaces at temperatures below 335 °C (0.5% Zn in fuel) and 472 °C (50% of Zn in fuel) [8]. This can explain the occurrence of zinc in the FeCr coating at the leeward side, where the minimum temperature during the exposure was 331 °C and zinc may have reacted with the iron oxide layer, forming $ZnCl_2$, causing accelerated corrosion.

At the higher temperature, clear differences between the coatings emerged: tube material A263 together with NiCr and NiCrTi coatings were the top performers. The corrosion rate for A263 was 1 μm/1000 h in the windward side and 9 μm/1000 h for the leeward side. For coatings, the corrosion rates varied between 5–22 μm/1000 h (windward) and 2–235 μm/1000 h (leeward). Zinc together with sulfur was detected on A263 material in the leeward side, where the corrosion attack was more pronounced compared to the protective oxide layer in the windward side. This is well in accordance with a previous study with zinc compounds, in which zinc is predicted to form sulfates in oxidizing conditions [7].

The amount of chromium in the composition of nickel based coatings was significant for the corrosion resistance at 750 °C. NiCr and NiCrTi coatings with 46 wt.% Cr showed very high corrosion performance, whereas NiCrW and IN625 corroded severely in the conditions, Figure 12. Even though FeCr coating contained less than 25 wt.% Cr, it showed better corrosion resistance in the boiler exposure. FeCr coating had high amounts of refractory metals niobium and tantalum. On the other hand, the amount of molybdenum, which can degrade by metal dusting at temperatures over 700 °C, was lower compared to NiCrW and IN625. The corrosion mechanism may also have changed from the lower temperature (550 °C) to the higher temperature (750 °C). Chlorine-activated corrosion was detected in the FeCr coating at 550 °C, but at 750 °C strong reactions of sulfur with nickel were observed. In a corrosion mechanism, the type of attack can change from salt molten attack to gaseous attack, which has strong influence on the corrosion rate [13]. In the case of NiCrW and IN625, the corrosion started with pitting, and led to catastrophic corrosion, when the protective chromium oxide layer formation failed after consuming the chromium. Similar accelerated corrosion and selective corrosion have been reported for TP347H steel and IN625 weld overlay material in a biomass and a waste incineration plant [5,6]. It has been concluded that corrosion rate accelerates above steam temperatures of 540 °C and selective corrosion occurs when Zn-K-Cl forms a molten phase.

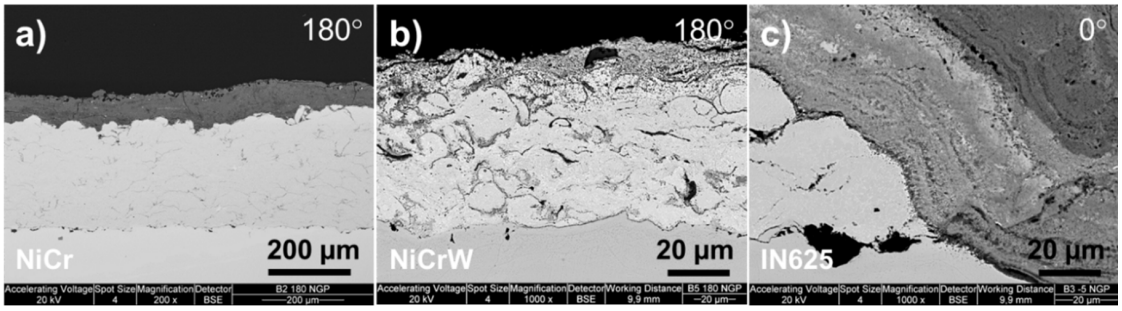

Figure 12. SEM (BSE) images of the HVOF Ni based coatings after exposure at 750 °C for 1300 h. Chromium content of the coatings varied from (**a**) NiCr with 46 wt.% Cr with deposit layer on top of the coating to (**b**,**c**) NiCrW and IN625 with 21 wt.% Cr.

In the future, studies with actual coated boiler tubes should be performed in order to validate the promising corrosion resistance of thermal spray coatings in biomass co-firing conditions at high temperatures.

Acknowledgments: This work was performed in the FP7 EU project NextGenPower—Efficiency increases in existing and new build pulverised coal power plants with a view to CCS. The authors would like to thank Alholmens Kraft Ab for the opportunity to use the power plant for the experiments.

Author Contributions: Maria Oksa conceived and designed the experiments; Janne Kärki performed the experiments; Maria Oksa, Jarkko Metsäjoki and Janne Kärki analyzed the data; Maria Oksa wrote the paper with the assistance of other authors.

Conflicts of Interest: The authors declare no conflict of interest. The founding sponsors had no role in the design of the study; in the collection, analyses, or interpretation of data; in the writing of the manuscript, and in the decision to publish the results.

References

1. The Paris Agreement. United Nations, 12 December 2015. Available online: http://unfccc.int/paris_agreement/items/9485.php (accessed on 19 September 2016).
2. 2030 Energy Strategy. Available online: https://ec.europa.eu/energy/en/topics/energy-strategy/2030-energy-strategy (accessed on 19 September 2016).
3. Technology Roadmap Wind Energy. Available online: https://www.iea.org/publications/freepublications/publication/Wind_2013_Roadmap.pdf (accessed on 19 September 2016).
4. Solar Photovoltaic Roadmap. Available online: https://www.iea.org/publications/freepublications/publication/pv_roadmap_foldout.pdf (accessed on 19 September 2016).
5. Montgomery, M.; Jensen, S.A.; Borg, U.; Biede, O.; Vilhelmsen, T. Experiences with high temperature corrosion at straw-firing power plants in Denmark. *Mater. Corros.* **2011**, *62*, 593–605. [CrossRef]
6. Montgomery, M.; Hansson, A.N.; Jensen, S.A.; Vilhelmsen, T.; Nielsen, N.H. In situ corrosion testing of various nickel alloys at Måbjerg waste incineration plant. *Mater. Corros.* **2013**, *64*, 14–25. [CrossRef]
7. Bankiewicz, D.; Vainikka, P.; Lindberg, D.; Frantsi, A.; Silvennoinen, J.; Yrjas, P.; Hupa, M. High temperature corrosion of boiler waterwalls induced by chlorides and bromides—Part 2: Lab-scale corrosion tests and thermodynamic equilibrium modeling of ash and gaseous species. *Fuel* **2012**, *94*, 240–250. [CrossRef]
8. Enestam, S.; Backman, R.; Mäkelä, K.; Hupa, M. Evaluation of the condensation behavior of lead and zinc in BFB combustion of recovered waste wood. *Fuel Process. Technol.* **2013**, *105*, 161–169. [CrossRef]
9. Oksa, M.; Auerkari, P.; Salonen, J.; Varis, T. Nickel-based HVOF coatings promoting high temperature corrosion resistance of biomass-fired power plant boilers. *Fuel Process Technol.* **2014**, *125*, 236–245. [CrossRef]
10. Oksa, M.; Metsäjoki, J. Optimizing NiCr and FeCr HVOF coating structure for high temperature corrosion protection applications. *J. Therm. Spray. Technol.* **2015**, *24*, 436–453. [CrossRef]
11. Hussain, T.; Dudziak, T.; Simms, N.J.; Nicholls, J.R. Fireside corrosion behavior of HVOF and plasma-sprayed coatings in advanced coal/biomass co-fired power plants. *J. Therm. Spray. Technol.* **2013**, *22*, 797–807. [CrossRef]

12. Oksa, M.; Kärki, J.; Metsäjoki, J. *Coating Solutions against High Temperature Corrosion-Performance Validation and Feasibility at Biomass Fired Boilers*; Pertti, A., Juha, V., Eds.; VTT Technology: Espoo, Finland, 2013; pp. 656–670.
13. Oksa, M.; Tuurna, S.; Varis, T. Increased lifetime for biomass and waste to energy power plant boilers with HVOF coatings: High temperature corrosion testing under chlorine-containing molten salt. *J. Therm. Spray. Technol.* **2013**, *22*, 783–796. [CrossRef]